#### **Research Article**

Irfan, Ming Hu\*, Lingyu Meng, and Chenxi Shi

# Laser re-melting of modified multimodal Cr<sub>3</sub>C<sub>2</sub>-NiCr coatings by HVOF: Effect on the microstructure and anticorrosion properties

https://doi.org/10.1515/rams-2023-0127 received January 23, 2023; accepted September 19, 2023

Abstract: Modified multimodal (MMP) Cr<sub>3</sub>C<sub>2</sub>-NiCr coatings were fabricated by high-velocity oxy-fuel (HVOF) spraying deposited on a CuCrZr alloy substrate. However, due to the lack of its inevitable porosity, an additional laser remelting (LRM) approach is highly required to improve the coating performance. Therefore, the LRM technique is employed in this study to improve the microstructure properties of an MMP Cr<sub>3</sub>C<sub>2</sub>-NiCr coating by HVOF. Solidstate phase transformation from Cr<sub>3</sub>C<sub>2</sub> to Cr<sub>7</sub>C<sub>3</sub> occurred during the LRM process. After the LRM process, the coating exhibits the presence of Cr<sub>3</sub>C<sub>2</sub> nanoparticles that serve as reinforcement. These nanoparticles demonstrate minimal lattice misfit and exhibit high stability throughout the LRM process. The surface of the coating undergoes modification, resulting in the formation of homogeneous nano (20–130 nm), micron (150 nm to 0.3  $\mu$ m), and submicron (2–3  $\mu$ m) Cr<sub>3</sub>C<sub>2</sub> structures, along with high-density microstructures, after the LRM process. Nano-Cr<sub>3</sub>C<sub>2</sub> particle reinforced with high total work function and incredibly increased corrosion rate significantly improves coating corrosion resistance. Overall, porosity decreased from 3.9% of the HVOF coating to 0.3% of the LRM. As a result, the current density of anticorrosion decreased from 33.7 to 4.35 μA·cm<sup>-2</sup>, and the Vickers microhardness average values ranged from 1,050 to 1,300 HV<sub>0.3</sub>, indicating improved microstructure development and related properties.

**Keywords:** HVOF, LRM, modified-multimodal coatings, Cr<sub>3</sub>C<sub>2</sub>–NiCr, microstructure, anticorrosion properties

**Irfan, Lingyu Meng, Chenxi Shi:** Jiamusi University College of Materials Science and Engineering, Jiamusi City, 154007, China

# 1 Introduction

Modern surface engineering development has continually attracted scientists' interest due to its unique advantages, such as improvement in the appearance of the substrate surface, enhancement in the microstructural properties, environmental protection damage, and mechanical properties. Several thermally sprayed metal coating techniques such as high-velocity oxy-fuel (HVOF), oxy-fuel wire, high-velocity air-fuel, oxy-fuel powder, electric arc wire, and plasma arc powder indicate major industrial solutions to protect surfaces from environmental damages [1–4].

The present study uses CuCrZr alloy as a substrate because of its widespread use in the optical, marine, automotive, and electrical equipment sectors. However, poor wear resistance and low hardness continue to limit industrial applications of copper [5,6]. Thus, there is a growing interest in improving copper alloy surface properties by employing surface coatings [7]. Using a thermal spraying method, surface-coated materials' most common industrial choices are compositions based on chromium carbides (Cr<sub>3</sub>C<sub>2</sub>) and/or tungsten carbides (WC). Compared to Cr<sub>3</sub>C<sub>2</sub>, the application of WC-based coating is limited to work below 500°C temperature due to its low thermal expansion coefficient and oxidation resistance [8]. However, in contrast to WCbased composites, Cr<sub>3</sub>C<sub>2</sub>-based compositions (i.e., Cr<sub>3</sub>C<sub>2</sub>-NiCr) can be operated at 800–900°C due to the high oxidation resistance [9]. Furthermore, the Cr<sub>3</sub>C<sub>2</sub>-based coating shows excellent resistance against corrosion in alkaline, chloride, and acidic (sulfuric and nitric) environments [10–12]. Therefore, Cr<sub>3</sub>C<sub>2</sub>-based composition is the first choice for applications such as high-temperature surface protection services, pump housing, valve stem, or spindle services compared to WCbased composition coating. In addition, another important reason to replace WC-based hard metal coatings with Cr<sub>3</sub>C<sub>2</sub>based coatings is its low cost.

Among  $Cr_3C_2$ -based compositions,  $Cr_3C_2$ -NiCr is the widely used chromium-based nanocomposite due to their valuable applications of wear protection, which can be

<sup>\*</sup> Corresponding author: Ming Hu, Jiamusi University College of Materials Science and Engineering, Jiamusi City, 154007, China; Metal Wear Resistant Materials and Surface Technology Engineering Research Center in the Ministry of Education, Jiamusi, 154007, China, e-mail: minghu02@jmsu.edu.cn

found in various fields such as chemical plant, petroleum, aerospace, and automotive services [13–15]. As mentioned above, the microhardness and corrosion resistance properties of the Cr<sub>3</sub>C<sub>2</sub>–NiCr composition system are suitable for surface coatings that can protect them from environmental damage and can improve the lifetime of the surface-coated materials, where WC-based compositions (WC-Co or WC-Ni) cannot be used. Many researchers even projected using Cr<sub>3</sub>C<sub>2</sub>–NiCr compositions as metal cutting tools due to their high hardness and low sintering temperatures [16,17].

Various thermal spraying methods are commonly used to coat chromium carbide composites. Among them, HVOF is the widely used method to enhance the surface properties of the base materials. The HVOF process is continuous and convenient for applying coatings to industrial installations at the site. HVOF-sprayed coatings, including cermet and anticorrosion alloys, have been subject to seawater corrosion testing. However, because of the spraying process, the HVOF deposits present a poorly melted state of chromium-based compositions (not all particles melted; un-melted hard particles were also found in the coating), indicating numerous porosities and cracks. This decreases the efficiency of their surface contact with the substrate's material, which leads to corrosion. Due to these disadvantages, HVOF is limited to some applications, particularly those that require more excellent resistance to wear, corrosion, and impact [18,19]. Therefore, an additional technique such as laser re-melting (LRM) is necessary to improve the surface engineering microstructure and corrosion resistance properties.

Laser treatment is a successful process used in industrial production due to its advantages in high energy density and stability [20–22]. This technique has proven to be a practical process for creating carbides-reinforced coatings. Furthermore, it can improve the quality of thermal spray coatings. Their objective is to fuse, totally or partially, the ceramic layer so that the material becomes more homogeneous in the posterior solidification and the pores disappear [23–25]. In the literature, various studies have highlighted that the microhardness, microstructural densification, and wear-resistant properties of the thermally sprayed WC-based or Cr<sub>3</sub>C<sub>2</sub>-based cermet coatings processed by the LRM have been improved [23-29]. According to Janka et al. [30], the low-power operating laser avoids re-melting the coating, and it could cause another chromium-carbide layer, precipitating the supersaturated Ni-based composite. Therefore, as a whole, the microstructure retained the morphologies and distribution of the as-sprayed carbide coating with an additional layer of chromium carbide. Furthermore, Mateos et al. [26] stated that the tungsten-based carbide coating enhanced with random and unbalanced shape distribution, while a prominent dendrite

shape was also observed after LRM completion. Qin *et al.* [25] also observed that the compact microstructure of the columnar dendrites, equiaxed dendrites, and fine grain of the HVOF Cr<sub>3</sub>C<sub>2</sub>–NiCr coatings had been enhanced, which improved the corrosion and wear resistance, as well as the carbide morphologies, its distribution became it more random and irregular after LRM. Therefore, to develop the microstructure, corrosion resistance, and hardness of the Cr<sub>3</sub>C<sub>2</sub>–NiCr surface coating on a copper alloy substrate, here in this study, we have used LRM due to its sophisticated properties after the HVOF process.

Thus, the present work deals with LRM treatments after the HVOF technique, which is beneficial to tailor the surface coating of modified multimodal (MMP)  $Cr_3C_2$ -NiCr toward developing microstructure, corrosion resistance properties and enhancing surface microhardness. We hope that this versatile LRM technique after HVOF could solve the significant problems of surface engineering technology.

# 2 Materials and experimental methods

#### 2.1 Materials

All the materials are bought from commercial resources and used without further purification. The substrate used in this study is CuCrZr alloy (Cu  $\sim$  99.09, Cr  $\sim$  0.81, Zr  $\sim$  0.08, and other 0.02 wt%), with a corresponding production of RS2020045519, the standard of JB/T7598-2008, and a melting furnace number of C1000965. MMP Cr<sub>3</sub>C<sub>2</sub>–NiCr powder size exhibited dimensions, and 15–45  $\mu m$  distributions were obtained from Fujian Dilong Innovation Development Co., Ltd., China.

#### 2.2 Experimental methods

The X-ray fluorescence technique was used to find the chemical composition of MMP  $Cr_3C_2$ -NiCr powders, as listed in Table 1. Furthermore, focused ion beam analysis was

Table 1: Chemical composition of MMP Cr<sub>3</sub>C<sub>2</sub>-NiCr powder

Powder composite	Cr	С	Ni	Ce	Zr	La	0
Sample (wt%)	62.2	17.51	15.88	1.64	0.0012	0.0046	2.76

performed to cut a single powder particle, and the phase composition was measured by a D8 advanced X-ray diffractometer (XRD) Cu K $\alpha$  radiation of  $\lambda$  = 0.154056 nm analysis. SEM/EDS (Modal ZEISS sigma 300) was used for morphological studies and the proportion of the elements. Samples for SEM observation were prepared using standard mechanical polishing procedures associated with etching in agua regia at room temperature. The microstructure of the MMP Cr<sub>3</sub>C<sub>2</sub>-NiCr coating interfacial layer was also investigated by cross-sectional TEM (FEI TECHNI G2 F30 operated at 200 keV with a point-to-point resolution of 0.23 nm). TEM analysis specimens were prepared by mechanical grinding. polishing, and dimpling. Electron diffraction patterns and high-resolution TEM images were taken. For the porosity analysis, SEM images of the coating were placed into a common computer folder, and particles were counted and sized automatically within ImageJ (Image-Pro®Plus v 6.0). This macro converted raw images to a binary image (black indicating a particle and white being the background) using autothresholding and a "fill holes" command to blacken any internal white pixels in the interior of a particle. The macro outputted a list of the projected area, image coordinates, and circularity for each particle detected in the images. Measurement of the microhardness of the coating was performed using an HRD-1000TMC Vickers microhardness tester at 3 N for a loading time of 15 s. For each hardness profile along the depth direction of the coating, three repeat tests were performed (the spacing of each press mark was larger than 50 mm), and their averaged results were used. Electrochemical corrosion resistance measurements were made at room temperature, exposing 1 cm<sup>2</sup> in a three-electrode cell containing 3.5% NaCl solution using Versa STAT 3: Modal-400 version 2.60.6.

# 2.3 Coating preparation

The CuCrZr substrates were ultrasonically cleaned with acetone and sandblasted with  $Al_2O_3$ , sandblasting with pressure P manually by the pressure regulator  $\pm 0.2$  MPa with a distance of 1.0 cm to the sample surface. In all, 110  $\mu$ m alumina ( $Al_2O_3$ ) (Sandblasting Machine Ningbo Yinzhou Wuxiang Xinzhe Machinery Factory) particles were used for the sandblasting process, and the forward blasting speed was set at 3.5 mm·s<sup>-1</sup>. The surface roughness values after and before sandblasting Ra are 0.99 and 5.011  $\mu$ m. An HVOF spraying system (HV-80-JP, China) was used to prepare MMP Cr<sub>3</sub>C<sub>2</sub>–NiCr coatings of average 150  $\mu$ m thickness on the surface of the copper substrate. Kerosene and oxygen were used as fuel and powder carrier gases, respectively. Kerosene flow

and spray distance changed during the following orthogonal experiment design. The pressures of kerosene and oxygen were fixed at 19–23 (L·min<sup>-1</sup>) and 40–53 (L·min<sup>-1</sup>) during the spraying process, respectively.

LRM experiments were conducted on a JHM-1GX/Y-600 China laser processor under the inert gas (nitrogen gas flow 5–10  $\rm L\cdot min^{-1}$ ) to re-melt the whole surface area of the sprayed coating. A fully re-melted coating surface was achieved with 50–60% overlap between the neighboring tracks, laser power ranging from 200 to 500 W, a spotlight diameter of 3 mm, and a scanning rate of 10–12 mm·s<sup>-1</sup>. The coating thickness was kept constant with an average value of 100  $\mu$ m. The specimen was irradiated at an irradiation angle of 90°. Experiments under the same conditions were carried out with optimum process parameters. Coating samples were mounted on a moving numerically controlled X–Y table below the fixed laser processing head.

# 3 Results and discussion

# 3.1 Microstructure analysis

#### 3.1.1 MMP powders

Figure 1 displays the SEM analysis results, which revealed that the MMP Cr<sub>3</sub>C<sub>2</sub>-NiCr powders consisted of nano-sized grains (30-150 nm), submicron-sized grains (200 nm-0.3  $\mu$ m), micron-sized grains (3–5.3  $\mu$ m) of Cr<sub>3</sub>C<sub>2</sub>, as well as NiCr grains. The agglomerated structure was a multiscale chromium carbide and nickel carbide cermet core with a metal binder shell covered by submicron and nano-chromium carbide particles. The multimodal structure maintained three kinds of states. The first state is submicron Cr<sub>3</sub>C<sub>2</sub> grains embedded in the voids constructed by micron Cr<sub>3</sub>C<sub>2</sub> grains. The second state included NiCr binder phases and nano-Cr<sub>3</sub>C<sub>2</sub> grains embedded in the voids formed by submicron and micron Cr<sub>3</sub>C<sub>2</sub> grains, and the third state, nano-Cr<sub>3</sub>C<sub>2</sub> grains dispersed in NiCr metal binder phases. Furthermore, Cr<sub>3</sub>C<sub>2</sub> has a density of 6.68 g·cm<sup>-2</sup>, a melting point of 1,890°C, and a boiling point of 3,800°C, making it an excellent wear-resistant coating due to its exceptional resistance to erosion and corrosion.

In addition, Figure 1(c)–(e) shows the aggregation of  $Cr_2C_3$  particles of different sizes used as feeding powders. The cross-sectional analysis reveals that the cross-section of the single particles is more compact and denser. In Figure 1(e), at high magnification, the surface of the single particle appears to be composed of a tiny nano- $Cr_2C_3$  modifier.

In addition, Figure 1(f) shows that EDS analysis confirms that these feeding powders will retain part of the oxygen and deposit it on the surface of the substrate during the spraying process. During the deposition process, an amount of the gas can be squeezed out, while a small part of the gas cannot be removed and remains in the coating, causing porosity on the surface. A few gaps or cracks form if this part of the oxygen is retained in the combined amount of the Cr<sub>2</sub>C<sub>3</sub> particles and the NiCr binder phase. Due to rapid heating and cooling stages during HVOF coating, the melted NiCr phase is hard to flow and fill the voids among the feed particles.

#### 3.1.2 Phase analysis for MMP powders and coatings

Figure 2 shows the XRD spectra of the MMP  $Cr_3C_2$ -NiCr powder and its corresponding HVOF and LRM coatings. Each XRD spectrum mainly consists of the hard particles of  $Cr_3C_2$  with orthorhombic (Pnma, 62) structured phase (reference PDF#71-2287) and a small amount of NiCr and tiny  $Cr_7C_3$  phases. The broadening of the  $2\theta$  around  $46^\circ$  and  $51.5^\circ$  diffraction peaks in the XRD spectrum of  $Cr_3C_2$ -NiCr powder indicates the presence of nano and submicron

 $\text{Cr}_3\text{C}_2$ . After HVOF, the newly emerged  $\text{Cr}_3\text{C}_2$ -NiCr coating broadening of the  $(2\theta=41.1-44.6^\circ)$  diffraction peak in the XRD spectral line indicates the presence of nanocrystallite NiCr; it is clear that the peak shifted with minor angle  $(2\theta=0.1\rightarrow0.6^\circ)$ . Furthermore, the XRD peaks show that the content of  $\text{Cr}_7\text{C}_3$  increases after HVOF and LRM coatings, which suggests that the decomposition of a small amount of  $\text{Cr}_3\text{C}_2$  particles occurred during HOVF and LRM coatings. At high laser beam input energy and an oxidizing atmosphere, a solid-state reaction occurs, which leads to the decomposition of the initial phases, and the intensity of the other phases increases [31,32]

$$7Cr_3C_2 \rightarrow 3Cr_7C_3 + 5C,$$
 (1)

$$C + O \rightarrow CO_2. \tag{2}$$

The diffraction peak broadening and  $50-52^{\circ}$  corresponding to  $2\theta$ , in the XRD spectra of  $Cr_3C_2$ –NiCr coating after LRM indicate the presence of nano and submicron  $Cr_3C_2$  and fine dendrite. Additionally, Figure 2 suggests a  $1-2^{\circ}$  broadening in the peak at  $42^{\circ}$ , corresponding to the  $2\theta$  angle. This broadening indicates that an excessive degree of supercooling occurred for the NiCr/Cr<sub>7</sub>C<sub>3</sub> phases, resulting in the development of a nanocrystalline phase due to rapid solidification [33].

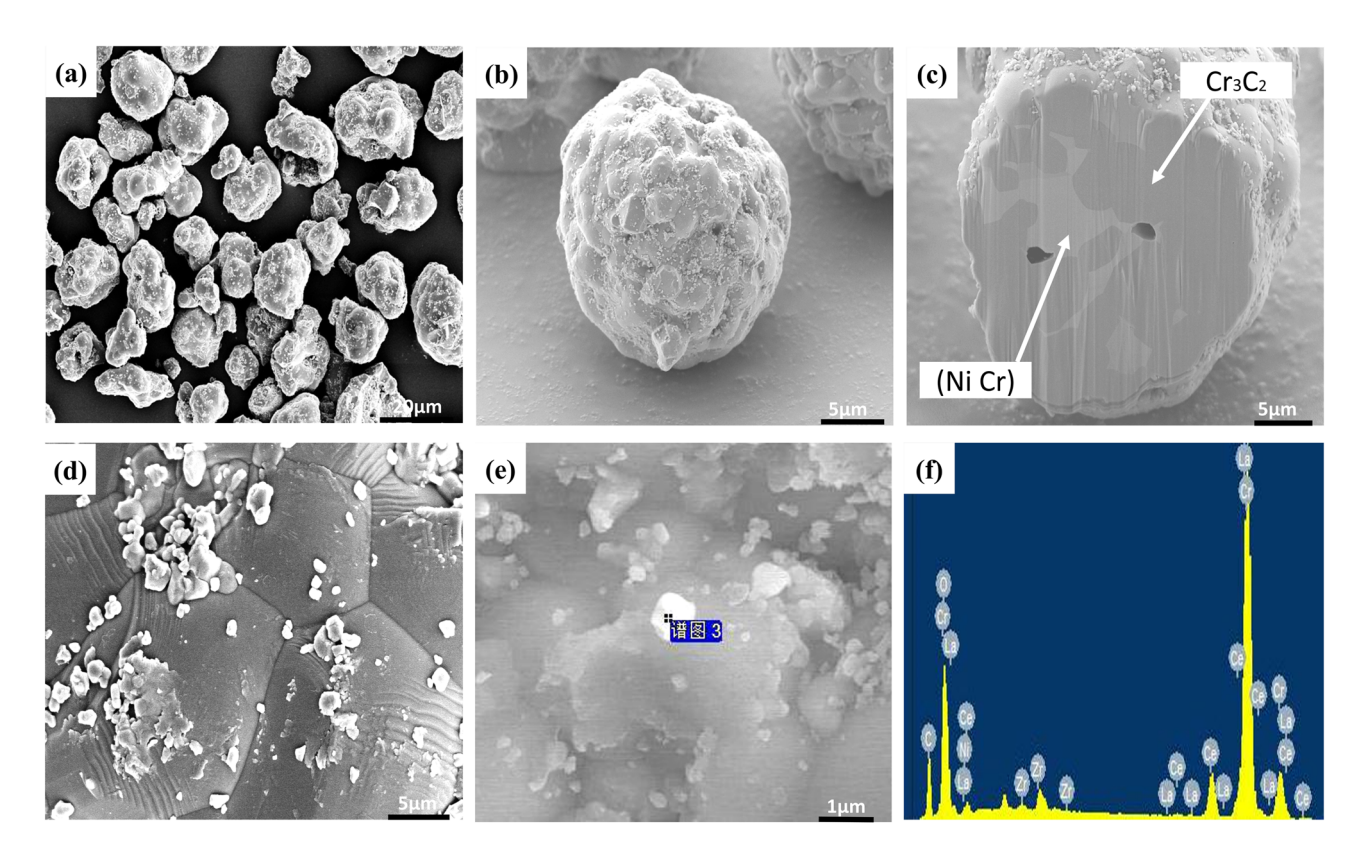


**Figure 1:** SEM/EDS of MMP  $Cr_3C_2$ -NiCr powder: (a) with low magnification, (b) single particle of the powder, (c) cross-sectional view of the single particle, and (d)–(f) with high magnification surface of the single particle.

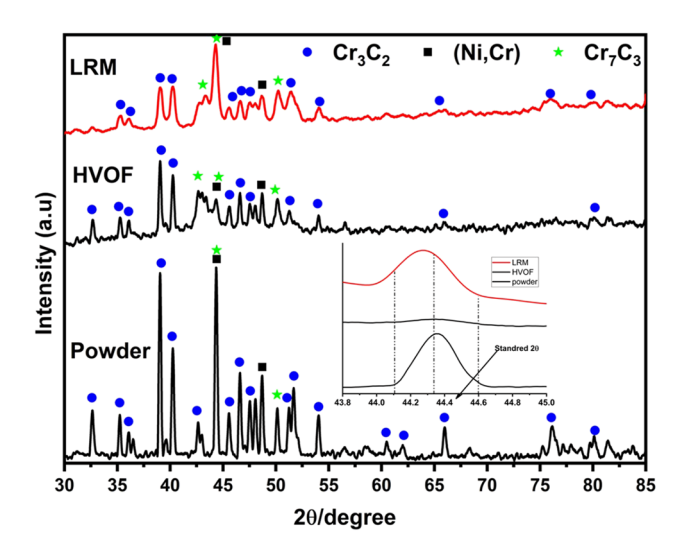


**Figure 2:** X-ray diffraction patterns of coating before and after LRM and powder.

#### 3.1.3 Microstructure analysis for MMP coatings

Figure 3 shows the SEM images of the MMP  $\rm Cr_3C_2-NiCr$  coating before and after the LRM process at different magnifications. Figure 3(a) and (c) shows that numerous dark

irregular particles of Cr<sub>3</sub>C<sub>2</sub> and its aggregates are unevenly distributed within the light gray NiCr binder phase. Additionally, several pores and cracks are present in the complete and NiCr phases, indicating a relatively low coating quality due to the selection of an inappropriate combination of spray process parameters.

Figure 3(b) and (d) shows that homogeneous and densified dendritic microstructures are formed during the LRM process. Some of the first dendrite grains have lengths ranging from 15 to 20 µm and are aligned along a specific direction. At higher magnification, the original irregular Cr<sub>3</sub>C<sub>2</sub> particles change into irregular square and long strips, clearly showing that some particles connect to form larger ones, and the edges and corners of the individual particles become smooth. The average length of the squares is 2-3 µm. Small irregular block structures combine in Figure 3(b) and (d). Figure 3(e)-(f) (EDS elemental analysis before and after LRM) shows that a small amount of rare earth exists in the coating besides C, Cr, and Ni elements. The LRM coating process exhibited a uniformly distributed carbide phase on the coating's surface. Depending on the amount of carbon in the carbide phase, different levels of dark gray are observed, as shown in Figure 3(d).

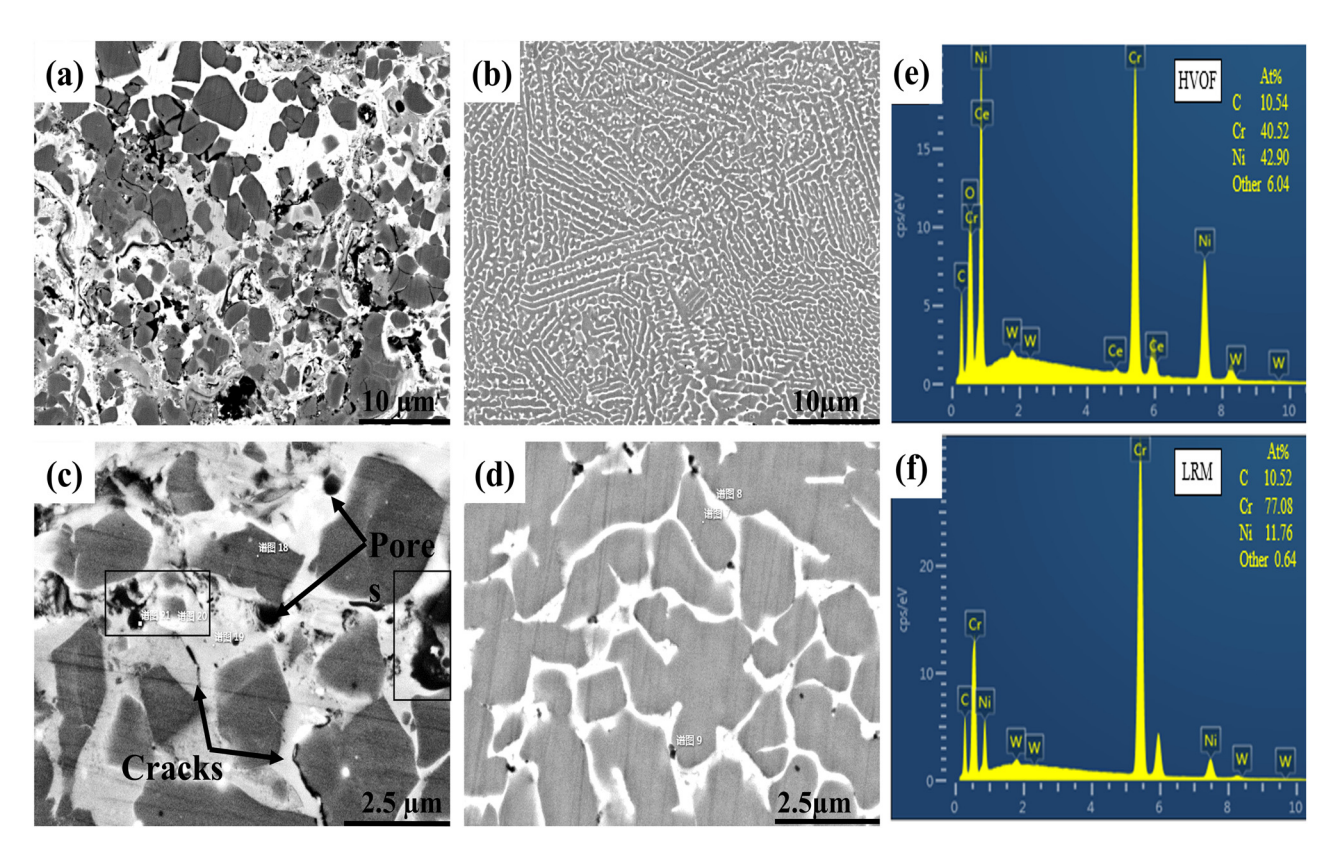


Figure 3: SEM images of the surface of HVOF coating (a) and (c) and after LRM coatings (b) and (d), and EDS results (e) HVOF and (f) LRM.

6 — Irfan et al. DE GRUYTER

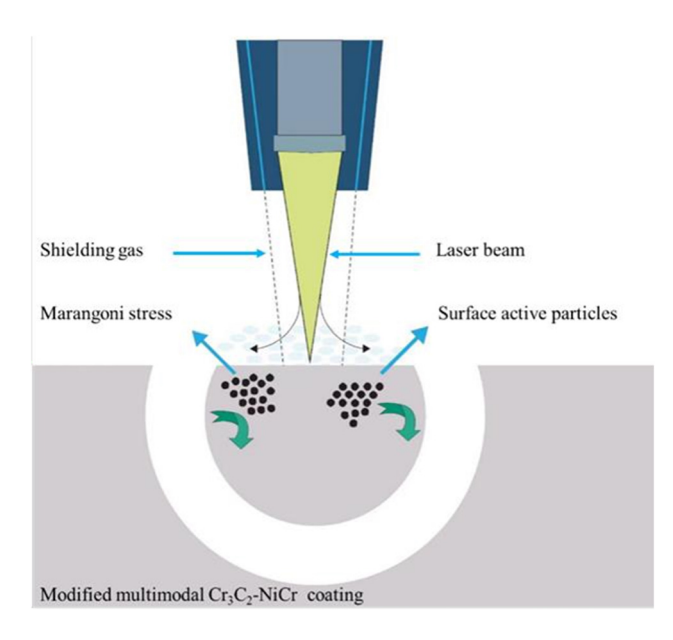


Figure 4: Sketch of the melt pool during the LRM process.

In addition, the LRM process generates Marangoni stress on the coating's surface due to the high energy flow through the laser beam. This stress arises from the surface tension gradient, gravity, and flexibility inside the molten pool caused by the high-frequency laser beam;

Figure 4 illustrates this phenomenon [14,34,35]. In this phenomenal situation during the LRM process, the un-melted particles of  $\rm Cr_3C_2$  and  $\rm Cr_7C_3$  start circulation and re-distribution in coating [36]. Moreover, during the LRM process, rare earth is added to the structure to refine it, reduce the surface tension of the liquid phase, decrease the interface energy between the metal and the coating, and increase the wettability and bonding strength. The adhesion strength of the coating after LRM (76.31  $\pm$  1.21 MPa) significantly improved compared to the HVOF coating (48.54  $\pm$  1.03 MPa). As a result, the LRM process effectively controls the distribution and size of carbides during their re-solidification and melting-growth period. This leads to improved microstructure properties, enhanced coating consistency, and increased resistance to corrosion.

MMP  $Cr_3C_2$ –NiCr coating refers to the microstructural states formed by the particle aggregates of micron, submicron, and nano carbides, as well as nanoparticles distributed in the molten binder phase after modification of nano-rare earth oxides. From Figure 5, the MMP  $Cr_3C_2$ –NiCr coating features remain after LRM, which provides the microstructural guarantee for good comprehensive coating performance. Figure 5 represents the elemental interdiffusion across the interface between the coating and substrate and was characterized through EDS analysis; the composition of the elements is listed in Table 2.

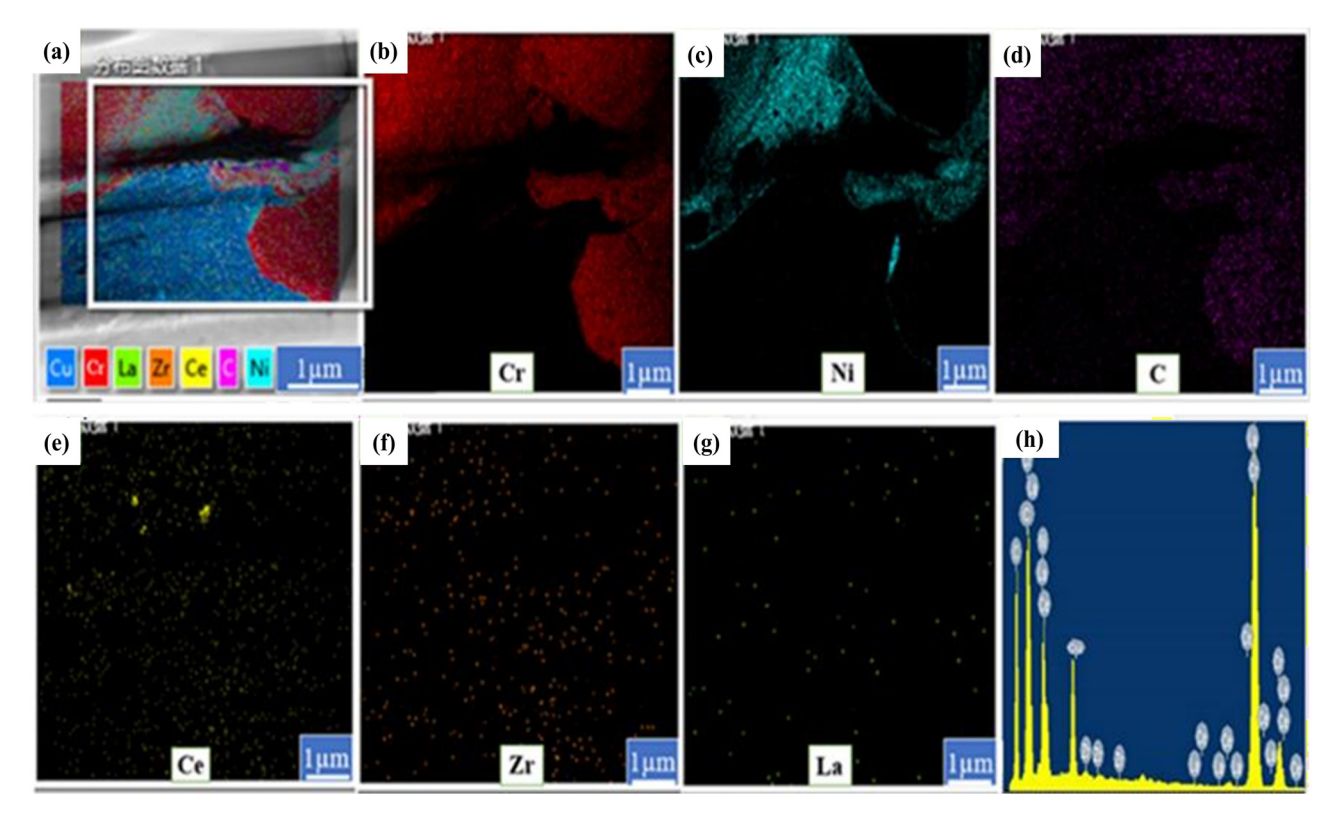


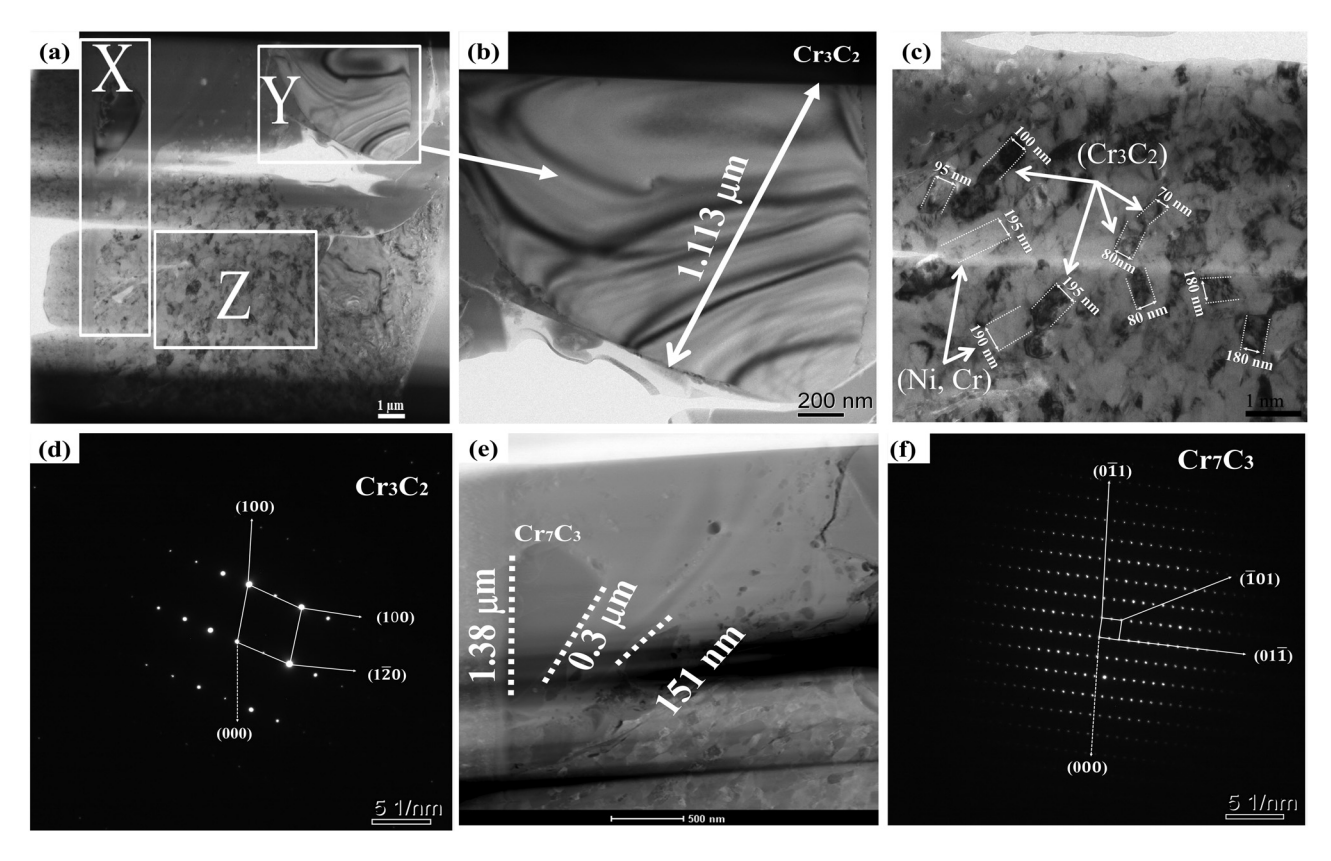
Figure 5: SEM/EDS analysis of cross-section interface/substrate after LRM (a)-(h).

Table 2: Elemental composition of the MMP Cr<sub>3</sub>C<sub>2</sub>-NiCr coating

Elements	Cu	Cr	С	Ni	Ce	Zr	La
Sample, wt%	11.21	62.41	16.21	3.94	2.45	2.20	1.58

For a further detailed analysis of the microstructural information, the bright-field images obtained through TEM and their corresponding selected area electron diffraction patterns are presented in Figure 6. Based on XRD and SEM analysis results and TEM diffraction patterns, it can be confirmed that both the lamella structure is Cr<sub>3</sub>C<sub>2</sub>. TEM images of the coating after the LRM process: the area mentioned in Figure 6 shows a cubic "Y" and with high magnification in Figure 6(b)–(d) is a Cr<sub>3</sub>C<sub>2</sub> crystallite with a size of 1.113 µm and a corresponding indexed diffraction pattern. The Cr<sub>3</sub>C<sub>2</sub> hard phase (PDF card#35-0804 orthorhombic (Pnam, 62)) precipitated in the coating during the LRM process. TEM and XRD have established that the coatings nano-micron and submicron grain structures retain, and their content remains unchanged. Furthermore, Figure 6 provides a detailed view of the interface/coating area, highlighted by a rectangle marked with an "X" in Figure 6(e) and (f). This area reveals the presence of strengthening Cr<sub>7</sub>C<sub>3</sub> phases (ranging from 0.3 to 1.38  $\mu m$ ) within the coating due to the LRM process. As mentioned earlier, the XRD spectra indicated an increase in the  $Cr_7C_3$  phases during the LRM process. TEM analysis further confirms this observation, which reveals that the coating primarily comprises nano- $Cr_3C_2$  and  $Cr_7C_3$  phases.

In Figure 6(a), marked with the rectangle labelled as "Z" and at high magnification in Figure 7(a), the inverse fast Fourier transform result in the insets of Figure 7(d) shows that the crystal phase was identified as NiCr, exhibiting a cubic structure (PDF#26-0429, Pm-3n (233)). It grows preferentially along the [1,2,0] direction with a d-spacing of 0.213 nm (as shown in Figure 7(b)). In Figure 7(c), several irregular elongated nano-crystallite phases with varying dimensions and shapes are visibly indicated. These long nanocrystalline phases are randomly dispersed throughout the MMP coating after the LRM process. Multiple crystalline phases, including Cr<sub>3</sub>C<sub>2</sub>, Cr<sub>7</sub>C<sub>3</sub>, and NiCr, are confirmed and marked within a rectangle in Figures 6(a) and 7(c). Those crystalline phases constituted multiple crystal forms with different dimensions, shapes, and orientations, thus producing various diffraction spots. This observation reinforces the presence of nanocrystalline carbide particles in the MMP Cr<sub>3</sub>C<sub>2</sub>-NiCr coating after the LRM process. These particles exhibit a size range from nano to micron to submicron dimensions. The sizes vary as follows: Cr<sub>3</sub>C<sub>2</sub> (70–190 nm), NiCr (190–195 nm), and  $Cr_7C_3$  (151 nm to 1.38  $\mu$ m). The presence of



**Figure 6:** (a) Cross-sectional TEM images of MMP  $Cr_3C_2$ -NiCr coating after LRM and (b)-(c)  $Cr_3C_2$  with high magnification (d)  $Cr_3C_2$  with the indexed diffraction pattern, (e)  $Cr_7C_3$  with high magnification and (f)  $Cr_7C_3$  with the indexed diffraction pattern.

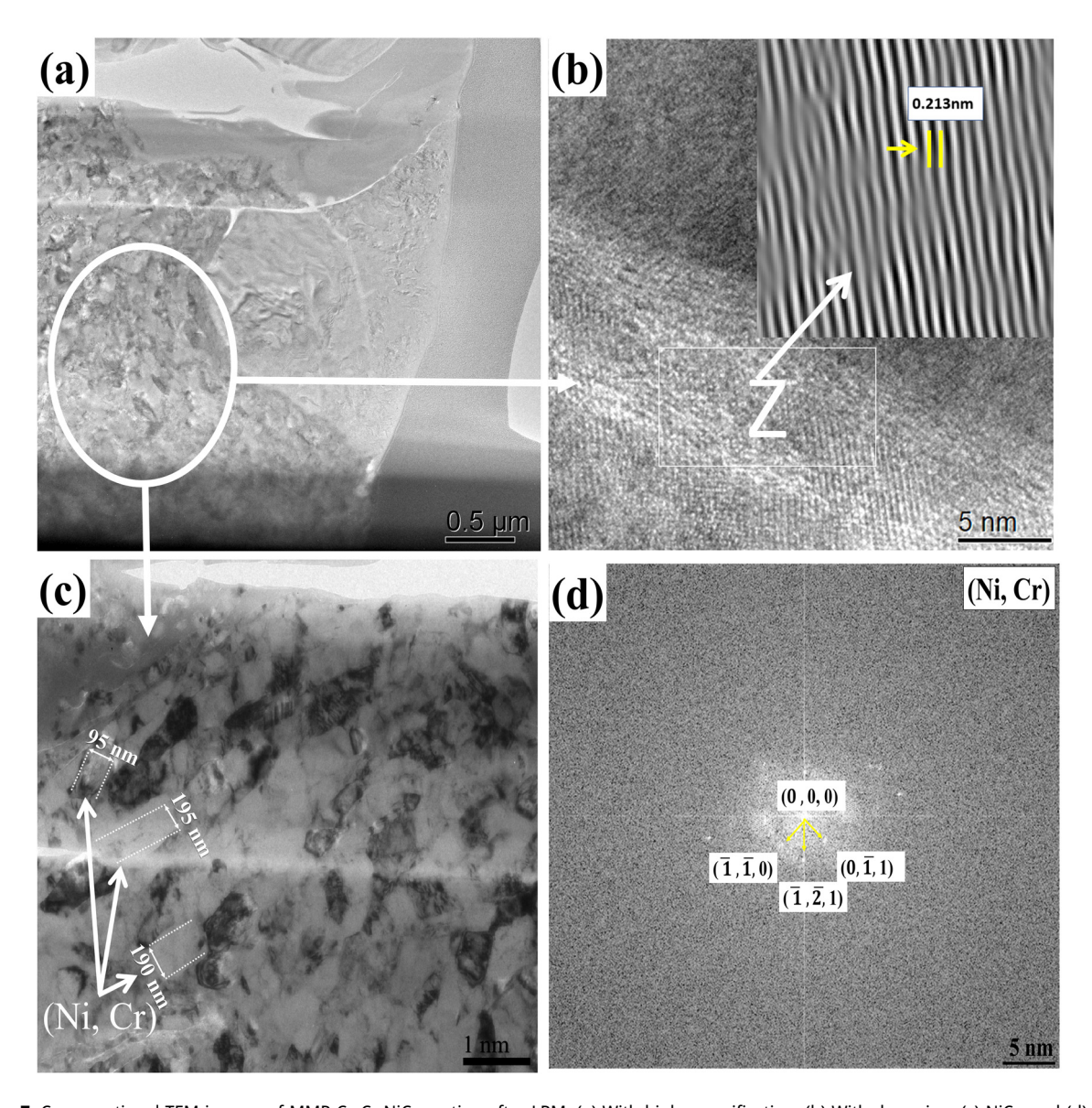


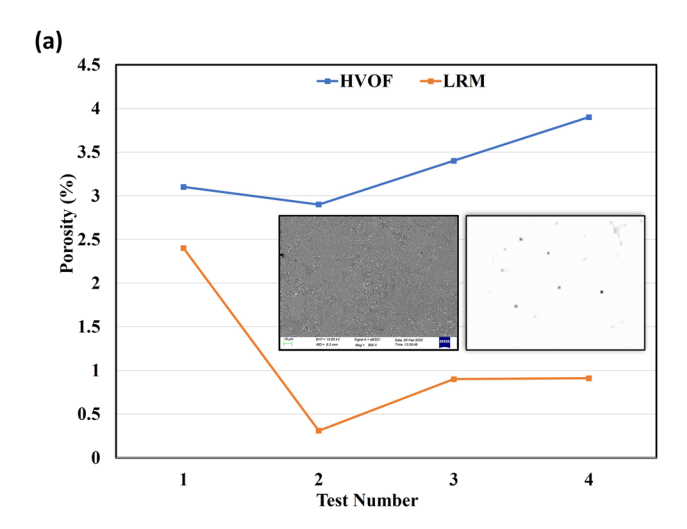
**Figure 7:** Cross-sectional TEM images of MMP Cr<sub>3</sub>C<sub>2</sub>-NiCr coating after LRM: (a) With high magnification, (b) With d-spacing, (c) NiCr, and (d) (IFFT) inverse fast Fourier transform.

nanoparticles in the coating formulation improved the mechanical and anticorrosion properties of the coating.

#### 3.2 Microhardness

The porosity results of the MMP  $Cr_3C_2$ —NiCr coating before and after the LRM process are depicted in Figure 8(a). The porosity investigation aims to determine the pore volume, considering the average pore size and its circularity [31]. Recent research on laser-molten nanocomposite carbides has revealed that evaporation can influence the elements' portion due to local solid laser power inputs [34]. As the laser power increases from 300 to 400 W and 500 W, the

material polymerizes, increasing total porosity due to structural changes and gasified decomposition of the  $Cr_3C_2$ –NiCr collecting  $O_2$  within the pores of the coating. After the LRM process, the porosity ratio reduces with various laser parameters due to each material system component's variable boiling and melting temperatures. High porosity values were discovered with a high laser power of 500 W with a scanning speed of  $12 \, \text{mm·s}^{-1}$ ; however, the porosity ratio reduced with a decrease in laser power to  $300 \, \text{W}$  with a scanning speed of  $10 \, \text{mm·s}^{-1}$ . The porosity decreased from 3.9% of the HVOF coating to 0.3% of the LRM process. The increase in porosity adversely affects the ductility and tensile strength of the coating. This negative impact can be attributed to reduced porosity hardness, resulting in a



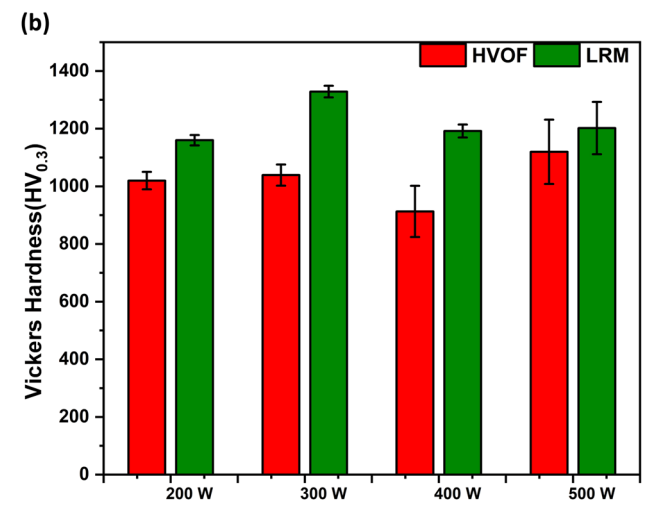


**Figure 8:** (a) The average porosity of the coatings (%) before and after LRM. (b) Vickers hardness  $HV_{0.3}$  before and after LRM.

decline in coating density [37]. Archimedes water displacement method obtained the density coating before and after the LRM process with average values of 3.552and 6.552 g·cm<sup>-3</sup>, respectively.

The microhardness of the coating surface before and after LRM was measured by an HXD-1000TMC digital microhardness tester with a load of 3 N and a dwelling time of 15 s. In Figure 8(b), it is observed that after LRM, the values of the Vickers hardness increased respectively. However, the average Vickers hardness of the HVOF coating is approximately 1,050 HV $_{0.3}$ , while after LRM, the values of the hardness increase gradually with the average values of 1,050–1,300 HV $_{0.3}$ . LRM, the solidified coating layer, is easier to re-melt and primarily affected by heat. If there are any tiny pores or cracks, they will disappear due to sufficient energy. In addition, high laser energy makes the bonding phase melt into liquid, filling the pores in the coating and improving the density of the coating.

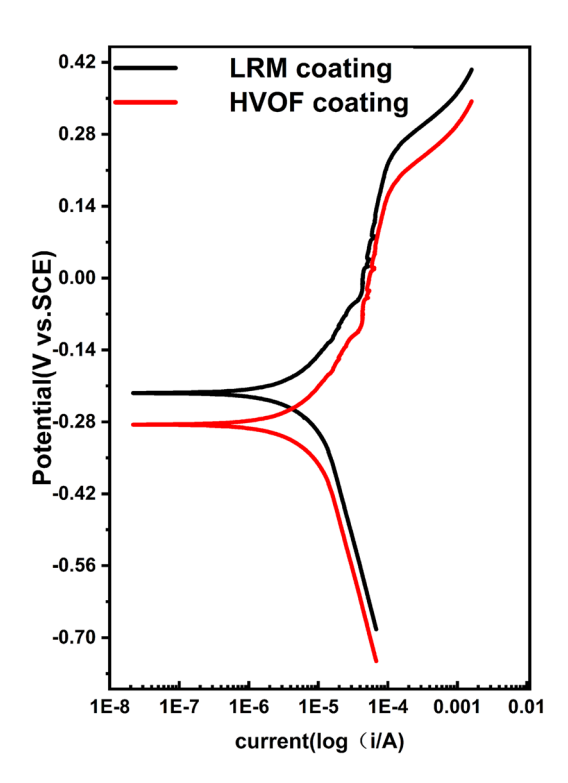


Figure 9: Potentiodynamic polarization plots of the HVOF sprayed and LRM.

Table 3: Comparison of the corrosion HVOF and LRM

S/No	E <sub>corr</sub> (V)	βα (V)	βc (V)	I <sub>corr</sub> (μA·cm <sup>-2</sup> )
HVOF coating	0.171	0.594	0.686	33.794
After LRM	0.064	1.458	4.854	4.35

### 3.3 Corrosion-resistant analysis

# 3.3.1 Corrosion-resistant phenomena

Figure 9 illustrates a comprehensive analysis of the potentiodynamic polarization resistance for HVOF and LRM coatings. The information includes Tafel plots and corresponding data presented in Table 3. Additionally, Eq. (3) (Stern-Geary) was utilized to evaluate the results and further understand the corrosion behavior of the coatings

$$Rp = \frac{\beta a^* \beta c}{2.3 \times I_{corr}(\beta a + \beta c)}$$
 (3)

In the Stern-Geary equation,  $\beta a$  represents the slope of the anodic branch,  $\beta c$  shows the cathodic slope, " $E_{\rm corr}$ " is the corrosion potential, and " $I_{\rm corr}$ " is the corrosion current density. The corrosion rate of the coating after LRM is eight times less than before LRM.

By solving Eq. (3) for the experimental data results, the value of the corrosion current density " $I_{corr}$ " of the

0 — Irfan et al. DE GRUYTER

 ${\rm Cr_3C_2}$ –NiCr coating after LRM measured at about 4.35–4.733  ${\rm \mu A \cdot cm^{-2}}$ , which is less than before 33.7  ${\rm \mu A \cdot cm^{-2}}$  measured for HVOF. LRM increases the density of the coating, leading to the blockage of the immersion path of the corrosion solution, improving the corrosion resistance. Furthermore, the decrease of corrosion current density after LRM is related to the homogenization of microstructure, and the obtained result proves that using the LRM process after HVOF is highly significant to deposit better quality of MMP  ${\rm Cr_3C_2}$ –NiCr-based coating on a substrate, which can operate in corrosive industrial application.

The occurrence of pitting corrosion should be because the electrode potential of a specific phase is relatively low, and the LRM changes or increases the electrode potential of the phase, as mentioned earlier in Table 3. The formation of oxide film improves the uniform corrosion ability of the coating [38]. Furthermore, some nickel ions diffuse into the formed oxide layer, accelerating the protective coating layer's formation and improving pitting corrosion resistance. Metals may have active, passive, or active-passive electrochemical behavior depending on the metal and environment. Active–passive metal NiCr shows active–passive and trans-passive regimes on the anodic polarization [39]. Research studies suggest that in Cr and Ni in  $Cr_3C_2$ –NiCr coatings, NiCr could form a corresponding passive layer of chromium to control corrosion [3,40].

Compared to the HVOF coating, the LRM process resulted in a positive shift in the corrosion potential. Additionally, it was observed that the passive current density decreased after the LRM process. In comparison, MMP Cr<sub>3</sub>C<sub>2</sub>-NiCr coating after the LRM process is composed of nano, submicron, micron Cr<sub>3</sub>C<sub>2</sub> grains, NiCr grains, and a tiny number of modifiers. The agglomerated structure consisted of a multiscale chromium and nickel carbide cermet core, with a surrounding shell of a metal binder, further covered with submicron and nano-chromium carbide particles. The nanoparticles turn into inert physical barriers to the initiation and development of corrosion, improving the corrosion resistance of the coating. According to the electrochemical corrosion principle, the larger the corrosion potential is, the smaller the current density is, the corrosion tendency of the materials is, and the better the corrosion resistance [39,41]. Some of the research investigations confirmed that the corrosion resistance of Cr<sub>3</sub>C<sub>2</sub>-NiCr coatings is the result of oxide formation, such as Cr<sub>2</sub>O<sub>3</sub> and Ni<sub>2</sub>O<sub>3</sub>, protecting the substrate from the corrosion resistance and enhancing the lifetime of the substrates [42].

#### 3.3.2 Corrosion mechanism

Electrochemical resistance mechanisms include anodic (which is oxidation) as well as cathodic (reduction) NaCl

[Na<sup>+</sup>, Cl<sup>-</sup>] [43]. The decomposition of a metal M is an anodic reaction:

$$M \to M^{n+} + ne^-. \tag{4}$$

For corrosion to occur, the anodic reaction's electron must be consumed by a cathodic reaction. The two most prevalent cathodic reactions in aqueous corrosion are oxidation and reduction [44]. An electron generated by the anodic reaction is consumed at the cathode (Eq. 5 shows that the reaction occurs),

$$Cr \rightarrow 2e^- + Cr^{2+}$$
. (5)

The presence of the nano, micron, and submicron particles after modification of the coating with the LRM process regulates materials on the nanoscale. It more effectively develops the potential of the materials' properties. This can be strongly reflected in the above microstructure analysis of the coating, which shows the decrease of the interface between the substrate and MMP  $\text{Cr}_3\text{C}_2$ –NiCr coating after the LRM process. In addition, by improving the nanostructure of the coating through nano-modification by the LRM process, anticorrosion properties increase.

# 4 Conclusions

In conclusion, modified multimodal Cr<sub>3</sub>C<sub>2</sub>–NiCr coatings were deposited on the CuCrZr alloy substrate. Laser beam properties of LRM and their effect on surface modification of MMP Cr<sub>3</sub>C<sub>2</sub>–NiCr coatings prepared by HVOF spraying are investigated. The main conclusions are presented as follows:

- 1) After the LRM process, observed changes in the coating reveal a distinct transformation of the original irregular  $Cr_3C_2$  particles into irregular square and long strips. Moreover, certain particles tend to merge, resulting in the formation of larger particle aggregates. Furthermore, the edges and corners of the individual particles become noticeably smoother during the LRM process. The average length of the squares is 2–3  $\mu$ m. In addition, the laser beam accelerated the Marangoni flow, promoting carbide nucleation and their homogeneous distribution.
- 2) The HVOF MMP Cr<sub>3</sub>C<sub>2</sub>–NiCr coatings consist of nano-sized, submicron-sized, and micron-sized hard grains and metallic binder phases. During the LRM process, submicron grains of Cr<sub>3</sub>C<sub>2</sub> become embedded in the voids created by larger Cr<sub>3</sub>C<sub>2</sub> grains, while the nano-sized Cr<sub>3</sub>C<sub>2</sub> grains disappear within the NiCr metal binder phases.
- 3) The coating density was measured before and after the LRM process, with average values of 3.552 and 6.552 g·cm<sup>-3</sup>, respectively. Compared to the HVOF coating, the MMP Cr<sub>3</sub>C<sub>2</sub>–NiCr coating after the LRM process exhibits a uniform and

- dense structure free from apparent lamellar formations. Additionally, the porosity is reduced by approximately 0.31–0.9%.
- 4) The Vickers hardness test with a load of 3 N, LRM Vickers hardness (HV<sub>0.3</sub>) values approximately 1,300 HV<sub>0.3</sub>, while HVOF coating values approximately 1,050 HV<sub>0.3</sub>.
- 5) The corrosion resistance of the coating increased after LRM and the corrosion current density after LRM was found to be  $4.35\,\mu\text{A}\cdot\text{cm}^{-2}$ , whereas the current density of the HVOF coating was  $33.794\,\mu\text{A}\cdot\text{cm}^{-2}$ . The corrosion rate after the LRM of the coating decreases. The protective, homogeneous oxide layer was formed on the Cr<sub>3</sub>C<sub>2</sub>–NiCr surface, protecting the tested materials against corrosion.

**Acknowledgments:** The authors are grateful for the valuable help from the support of the National Natural Science Fund (No. 51671096) project of China and Professor Wang You from the Harbin Institute of Technology.

**Funding information:** This research was supported by National Natural Science Fund (No. 51671096) project of China and Professor Wang You from the Harbin Institute of Technology.

**Author contributions:** Ming Hu: contributed significantly to designing the conception of the study and conducted final approval of the manuscript. Irfan: performed the research, analyzed, and interpreted the collected data, and wrote the manuscript. Lingyu Meng: helped to perform the experiment. Chenxi Shi: contributed to carrying out additional analyses with constructive discussions. All authors have accepted responsibility for the entire content of this manuscript and approved its submission.

**Conflict of interest:** The authors state no conflict of interest.

**Data availability statement:** The datasets generated during and analyzed during the current study are available from the corresponding author upon reasonable request.

# References

- [1] Chong, K., Y. Zou, D. Wu, Y. Tang, and Y. Zhang. Pulsed laser remelting supersonic plasma sprayed Cr<sub>3</sub>C<sub>2</sub>-NiCr coatings for regulating microstructure, hardness, and corrosion properties. Surface and Coatings Technology, Vol. 418, 2021 Jul, id. 127258.
- [2] Ping, X. L., H. G. Fu, S. T. Sun, J. Lin, X. Y. Guo, and Y. P. Lei. Microstructure and performance of Nb-bearing Ni60A-Cr<sub>3</sub>C<sub>2</sub>

- coatings manufactured by laser cladding. *Surface Engineering*, Vol. 36, No. 12, 2020 Dec, pp. 1294–1306.
- [3] Sadeghimeresht, E., N. Markocsan, and P. Nylen. Microstructural characteristics and corrosion behavior of HVAF-and HVOF-sprayed Fe-based coatings. *Surface and Coatings Technology*, Vol. 318, 2017 May, pp. 365–373.
- [4] Zhu, L., S. Wang, H. Pan, C. Yuan, and X. Chen. Research on remanufacturing strategy for 45 steel gear using H13 steel powder based on laser cladding technology. *Journal of Manufacturing Processes*, Vol. 49, 2020 Jan, pp. 344–354.
- [5] Ni, J., J. Li, W. Luo, Q. Han, Y. Yin, Z. Jia, et al. Microstructure and properties of in-situ TiC reinforced copper nano-composites fabricated via long-term ball milling and hot pressing. *Journal of Alloys* and Compounds, Vol. 755, 2018 Jul, pp. 24–28.
- [6] Yang, F., Q. Qin, T. Shi, X. Lu, C. Chen, Z. Guo, et al. In-situ synthesis of TiC-Al<sub>2</sub>O<sub>3</sub> coating on copper surface. *Surface and Coatings Technology*, Vol. 373, 2019 Sep, pp. 65–74.
- [7] Bateni, M. R., F. Ashrafizadeh, J. A. Szpunar, and R. A. Drew. Improving the tribological behavior of copper through novel Ti–Cu intermetallic coatings. Wear, Vol. 253, No. 5–6, 2002 Sep, pp. 626–639.
- [8] Janka, L., L. M. Berger, J. Norpoth, R. Trache, S. Thiele, C. Tomastik, et al. Improving the high temperature abrasion resistance of thermally sprayed Cr<sub>3</sub>C<sub>2</sub>-NiCr coatings by WC addition. Surface and Coatings Technology, Vol. 337, 2018 Mar, pp. 296–305.
- [9] Wang, H., X. Yan, H. Zhang, M. Gee, C. Zhao, X. Liu, et al. Oxidation-dominated wear behaviors of carbide-based cermets: A comparison between WC-WB-Co and Cr<sub>3</sub>C<sub>2</sub>-NiCr coatings. *Ceramics International*, Vol. 45, No. 17, 2019 Dec, pp. 21293–21307.
- [10] Dzhurinskiy, D., A. Babu, P. Pathak, A. Elkin, S. Dautov, and P. Shornikov. Microstructure and wear properties of atmospheric plasma-sprayed Cr<sub>3</sub>C<sub>2</sub>-NiCr composite coatings. *Surface and Coatings Technology*, Vol. 428, 2021 Dec, id. 127904.
- [11] Wu, H. and D. Kong. Effects of laser power on friction–wear performances of laser thermal sprayed Cr<sub>3</sub>C<sub>2</sub>–NiCr composite coatings at elevated temperatures. *Optics & Laser Technology*, Vol. 117, 2019 Sep, pp. 227–238.
- [12] Yuan, J. M., T. S. Dong, B. G. Fu, G. L. Li, L. Liu, and R. Wang. Effect of Tungsten Inert Gas Arc Re-melting on Microstructure and Wear Properties of Plasma-Sprayed NiCr-Cr<sub>3</sub>C<sub>2</sub> Coating. *Journal of Materials Engineering and Performance*, Vol. 28, 2019 Oct, pp. 6320–6329.
- [13] Kumar, R., K. Goyal, and D. Bhandari. Slurry erosion behavior of thermally sprayed ceramic nano-composite coatings on turbine steel. *International Journal of Applied Ceramic Technology*, Vol. 19, No. 6, 2022 Nov, pp. 3049–3061.
- [14] Schwanekamp, T., G. Marginean, and M. Reuber. Laser beam melting of Cr<sub>3</sub>C<sub>2</sub>-NiCr. *International Journal of Refractory Metals and Hard Materials*, Vol. 85, 2019 Dec, id. 105069.
- [15] Sharma, A., A. Vijay, and F. Sadeghi. Finite element modeling of fretting wear in anisotropic composite coatings: Application to HVOF Cr<sub>3</sub>C<sub>2</sub>-NiCr coating. *Tribology International*, Vol. 155, 2021 Mar, id. 106765.
- [16] Singh, S., K. Goyal, and R. Bhatia. Mechanical and microstructural properties of yttria-stabilized zirconia reinforced Cr<sub>3</sub>C<sub>2</sub>-25NiCr thermal spray coatings on steel alloy. *Journal of Electrochemical Science and Engineering*, Vol. 12, No. 5, 2022 Oct, pp. 819–828.
- [17] Özer, A. and Y. K. Tür. Sintering behaviour and mechanical properties of Cr<sub>3</sub>C<sub>2</sub>-NiCr cermets. *Bulletin of Materials Science*, Vol. 36, 2013 Oct, pp. 907–911.

- [18] Qiao, Y., J. Huang, D. Huang, J. Chen, W. Liu, Z. Wang, and Z. Zhibin. Effects of laser scanning speed on microstructure, microhardness, and corrosion behavior of laser cladding Ni45 coatings. *Journal of Chemistry*, Vol. 2020, 2020 Aug, id. 1438473.
- [19] Zhang, J., J. Lei, Z. Gu, F. Tantai, H. Tian, J. Han, et al. Effect of WC-12Co content on wear and electrochemical corrosion properties of Ni-Cu/WC-12Co composite coatings deposited by laser cladding. Surface and Coatings Technology, Vol. 393, 2020 Jul, id. 125807.
- [20] Zhang, P., X. Zou, S. Zhang, C. Xia, C. Liang, N. Liu, et al. Improve the binding force of PEEK coating with Mg surface by femtosecond lasers induced micro/nanostructures. *Journal of Materials Science*, Vol. 56, No. 23, 2021 Aug, pp. 13313–13322.
- [21] Zhang, Y., X. Gao, X. Liang, K. Chong, D. Wu, and Y. Zou. Effect of laser re-melting on the microstructure and corrosion property of the arc-sprayed AlFeNbNi coatings. Surface and Coatings Technology, Vol. 398, 2020 Sep, id. 126099.
- [22] Chen, H. and D. Kong. Effects of laser re-melting speeds on microstructure, immersion corrosion, and electrochemical corrosion of arc-sprayed amorphous Al-Ti-Ni coatings. *Journal of Alloys and Compounds*, Vol. 771, 2019 Jan, pp. 584–594.
- [23] Mazaheri, Y., R. Malmir, M. M. Jalilvand, M. Sheikhi, and A. Heidarpour. Mechanical properties and tribological performance of A356/Cr<sub>3</sub>C<sub>2</sub>-NiCr surface composite developed by high-velocity oxy-fuel and post friction stir processing treatment. Surfaces and Interfaces, Vol. 28, 2022 Feb, id. 101627.
- [24] Panziera, R. C., A. C. de Oliveira, M. Pereira, and F. Ratszunei. Study of the effects of the laser re-melting process on the microstructure and properties of the WC-10Co-4Cr coating sprayed by HVOF. *Journal of the Brazilian Society of Mechanical Sciences and Engineering*, Vol. 42, 2020 Mar, pp. 1–8.
- [25] Qin, E., B. Wang, W. Li, W. Ma, H. Lu, and S. Wu. Optimized microstructure and properties of Cr<sub>3</sub>C<sub>2</sub>-NiCr cermet coating by HVOF/laser hybrid processing. *Journal of Thermal Spray Technology*, Vol. 28, 2019 Jun, pp. 1072–1080.
- [26] Mateos, J. J., J. M. Cuetos, E. Fernandez, and R. Vijande. Tribological behaviour of plasma-sprayed WC coatings with and without laser re-melting. Wear, Vol. 239, No. 2, 2000 Apr, pp. 274–281.
- [27] Chen, H., C. Xu, Q. Zhou, I. M. Hutchings, P. H. Shipway, and J. Liu. Micro-scale abrasive wear behaviour of HVOF sprayed and laser-remelted conventional and nanostructured WC–Co coatings. Wear, Vol. 258, No. 1-4, 2005 Jan, pp. 333–338.
- [28] Bolelli, G., L. M. Berger, T. Börner, H. Koivuluoto, V. Matikainen, L. Lusvarghi, et al. Sliding and abrasive wear behaviour of HVOFand HVAF-sprayed Cr<sub>3</sub>C<sub>2</sub>–NiCr hardmetal coatings. *Wear*, Vol. 358, 2016 Jul, pp. 32–50.
- [29] Zhang, H., K. Chong, W. Zhao, and Z. Sun. Effects of pulse parameters on in-situ Ti-V carbides size and properties of Fe-based laser cladding layers. *Surface and Coatings Technology*, Vol. 344, 2018 Jun, pp. 163–169.
- [30] Janka, L., J. Norpoth, S. Eicher, M. R. Ripoll, and P. Vuoristo. Improving the toughness of thermally sprayed Cr<sub>3</sub>C<sub>2</sub>-NiCr hard-metal coatings by laser post-treatment. *Materials & Design*, Vol. 98, 2016 May, pp. 135–142.

- [31] Du, J. Y., F. Y. Li, L. M. Wang, H. Y. Lu, X. J. Ran, and X. Y. Zhang. Influences of plasma arc re-melting on microstructure and service performance of Cr<sub>3</sub>C<sub>2</sub>-NiCr/NiCrAl composite coating. *Surface and Coatings Technology*, Vol. 369, 2019 Jul, pp. 16–30.
- [32] Magnani, M., P. H. Suegama, N. Espallargas, C. S. Fugivara, S. Dosta, J. M. Guilemany, et al. Corrosion and wear studies of Cr<sub>3</sub>C<sub>2</sub>-NiCr-HVOF coatings sprayed on AA7050 T7 under cooling. *Journal of Thermal Spray Technology*, Vol. 18, 2009 Sep, pp. 353–363.
- [33] Matthews, S., B. James, and M. Hyland. The role of microstructure in the high temperature oxidation mechanism of Cr<sub>3</sub>C<sub>2</sub>–NiCr composite coatings. *Corrosion Science*, Vol. 51, No. 5, 2009 May, pp. 1172–1180.
- [34] Schwanekamp, T., G. Marginean, M. Reuber, and A. Ostendorf. Impact of cobalt content and grain growth inhibitors in laser-based powder bed fusion of WC-Co. *International Journal of Refractory Metals and Hard Materials*, Vol. 105, 2022 Jun, id. 105814.
- [35] Arrizubieta, J. I., A. Lamikiz, F. Klocke, S. Martínez, K. Arntz, and E. Ukar. Evaluation of the relevance of melt pool dynamics in Laser Material Deposition process modeling. *International Journal of Heat and Mass Transfer*, Vol. 115, 2017 Dec, pp. 80–91.
- [36] Ott, D. K., W. Cyrs, and T. M. Peters. Passive measurement of coarse particulate matter, PM10–2.5. *Journal of Aerosol Science*, Vol. 39, No. 2, 2008 Feb, pp. 156–167.
- [37] Lemaitre, J. and R. Desmorat. Engineering damage mechanics: ductile, creep, fatigue and brittle failures. Springer Science & Business Media, 2006.
- [38] Guilemany, J. M., J. Fernandez, J. Delgado, A. V. Benedetti, and F. Climent. Effects of thickness coating on the electrochemical behaviour of thermal spray Cr<sub>3</sub>C<sub>2</sub>–NiCr coatings. *Surface and Coatings Technology*, Vol. 153, No. 2–3, 2002 Apr, pp. 107–113.
- [39] Li, X. and K. Ogle. The passivation of Ni-Cr-Mo alloys: time resolved enrichment and dissolution of Cr and Mo during passive-active cycles. *Journal of The Electrochemical Society*, Vol. 166, No. 11, 2019 May, id. C3179.
- [40] Dehgahi, S., R. Amini, and M. Alizadeh. Microstructure and corrosion resistance of Ni-Al<sub>2</sub>O<sub>3</sub>-SiC nano-composite coatings produced by electrodeposition technique. *Journal of Alloys and Compounds*, Vol. 692, 2017 Jan, pp. 622–628.
- [41] Yang, X., W. Fan, and Z. Li. A continuum damage model for prediction of crack initiation life of pitting corrosion and fatigue. *International Journal of Damage Mechanics*, Vol. 31, No. 6, 2022 Jun, pp. 797–814.
- [42] Feng, Q., T. Li, H. Teng, X. Zhang, Y. Zhang, C. Liu, et al. Investigation on the corrosion and oxidation resistance of Ni-Al<sub>2</sub>O<sub>3</sub> nano-composite coatings prepared by sediment co-deposition. Surface and Coatings Technology, Vol. 202, No. 17, 2008 May, pp. 4137–4144.
- [43] Li, S., Z. Guo, J. Xiong, Y. Lei, Y. Li, J. Tang, et al. Corrosion behavior of HVOF sprayed hard face coatings in alkaline-sulfide solution. *Applied Surface Science*, Vol. 416, 2017 Sep, pp. 69–77.
- [44] Sherif, E. M. and S. M. Park. Effects of 1, 4-naphthoquinone on aluminum corrosion in 0.50 M sodium chloride solutions. *Electrochimica Acta*, Vol. 51, No. 7, 2006 Jan, pp. 1313–1321.